An error indicator for finite difference methods using spectral techniques with application to aerofoil simulation

Christian T. Jacobs[a,*], Markus Zauner[a], Nicola De Tullio[a], Satya P. Jammy[a], David J. Lusher[a], Neil D. Sandham[a]

[a] *Aerodynamics and Flight Mechanics Group, Faculty of Engineering and the Environment, University of Southampton, University Road, Southampton, SO17 1BJ, United Kingdom*

Abstract

This work introduces a new error indicator which can be used to determine areas of insufficient numerical resolution in unfiltered finite difference simulations. The background behind the methodology is that smaller scales (i.e. the flow features with higher wave numbers) are physically characterised by a smaller energy content in comparison with larger scales. This energy should decrease with increasing wavenumber at a minimum rate; if this rate is not attained it likely means that the smaller scales are not being properly resolved on the computational grid of solution points. An approach using spectral techniques is used to formulate two varieties of the error indicator – one integer-valued and one floating point-valued. These values are computed at a finite number of 'blocks' which span the domain. The indicator is implemented within the OpenSBLI finite difference-based modelling framework, and evaluated in the context of a three-dimensional Taylor-Green

*Corresponding author.
E-mail address: C.T.Jacobs@soton.ac.uk

vortex problem and flow past a V2C laminar flow aerofoil.

Keywords: Error indicators, Finite difference methods

1. Introduction

Computational grids are at the core of many numerical models. They comprise a set of points upon which the governing equations are solved. One of the crucial constraints of grid generation is that small-scale structures must be sufficiently well resolved by the grid, since any errors (introduced through numerical dispersion and dissipation, as well as nonlinear effects such as aliasing) can cause the simulation to become inaccurate and unstable [1]. Adopting a uniformly-fine grid to ensure this constraint is satisfied often results in a large number of superfluous grid points, which is detrimental to the model's computational efficiency. At the same time, it is often not possible to know *a priori* exactly where high resolution needs to be placed in the domain, particularly when dealing with transient and turbulent dynamics frequently encountered in real-world applications. The formulation of *a posteriori* error estimators and indicators [2, 3, 4, 5, 6], and their coupling with adaptive grid refinement methods [7, 8, 9, 10, 11, 12, 13], has therefore attracted a considerable amount of attention over the last few decades.

The current work is focussed on finite difference solutions of the compressible Navier-Stokes equations in the absence of explicit filtering or artificial dissipation. Such an approach is commonly used for DNS [14]. A feature of under-resolved regions of flow is the appearance of grid-to-grid point oscillations, usually first apparent in derivative quantities such as vorticity or dilatation rate. Typically the appearance of such numerical errors/oscillations

is used to decide when and where grid refinement is required. This work aims to quantify and calibrate these features of under-resolution such that the grid refinement process can ultimately be automated.

A new error indicator, based on spectral techniques using small-domain Fourier transforms, is presented herein. It does not attempt to quantify the solution error, but instead estimates the severity of any under-resolution that occurs in the solution field. The indicator is implemented in the OpenSBLI finite difference modelling framework [15]. Section 2 describes the error indicator in further detail. It is then evaluated in Section 3 by considering three-dimensional simulations of the Taylor-Green vortex problem [16] and flow past a V2C laminar aerofoil (see e.g. [17]). Some conclusions are drawn in Section 5.

2. Error Indicator

The error indicator considers a finite number of small cubes which together span the whole 3D domain. For each N_e^3 block, and for each line of N_e points within it, various Fourier amplitudes of a user-specified solution field are computed. These amplitudes are subsequently averaged over N_e^2 lines to determine the anisotropic error 'severity' values.

The first step to computing the error indicator is to apply a Hamming window to the solution field y, in order to ensure its smoothness and periodicity for Fourier analysis. Thus for each line of N_e solution points in each direction:

$$y_j = y_j \frac{\left(0.54 - 0.46 \cos\left(\frac{2\pi j}{N_e}\right)\right)}{0.54}, \tag{1}$$

where y_j is the j-th component of the solution field y in the line of solution points under consideration.

The Fourier amplitudes (proportional to the square root of the spectral energy) for selected modes/wavenumbers $N_e/2$, $N_e/4$ and $N_e/8$ of the solution field are then computed, for each N_e^3 block. In order to avoid doing a computationally intensive Fourier transform each time, the amplitudes are reconstructed by using simple summations, S:

$$S_2 = \sum_{j=0}^{N_e-1} (-1)^j y_j, \tag{2}$$

$$S_4 = \sum_{j=0}^{N_e-1} (-\mathrm{i})^j y_j, \tag{3}$$

$$S_8 = \sum_{j=0}^{N_e-1} \exp(-\frac{\pi}{4}\mathrm{i})^j y_j, \tag{4}$$

where $\mathrm{i} = \sqrt{-1}$. These values were checked for correctness against a fast Fourier transform.

With an increasing mode/wavenumber k, we desire the spectral energy $E(k)$ (and therefore the mode amplitude $Y(k)$) to decrease at a minimum rate, such that the smallest scales have the lowest energy content. An increase in $E(k)$, for example due to aliasing errors arising from non-linear terms, is likely to mean that we are not resolving the small scales well enough. Determining where this increase occurs in the domain facilitates the dynamic focussing of resolution in that area. To this end, the error indicator presented here is based on detecting whether the spectrum decay rate is worse than some prescribed value.

Two versions of the error indicator, denoted I_i and I_f, were developed; I_i is integer-valued while the other, I_f, is floating-point-valued. These are defined as

$$I_i = \begin{cases} 1, & \text{if } A_2 > A_4 + \varepsilon \\ 0, & \text{otherwise} \end{cases} + \begin{cases} 1, & \text{if } A_4 > A_8 + \varepsilon \\ 0, & \text{otherwise} \end{cases} + \begin{cases} 1, & \text{if } A_2 > A_8 + \varepsilon \\ 0, & \text{otherwise} \end{cases} \tag{5}$$

$$I_f = \log\left(1 + \lfloor \frac{A_2}{A_4 + \varepsilon} \rfloor + \lfloor \frac{A_4}{A_8 + \varepsilon} \rfloor + \lfloor \frac{A_2}{A_8 + \varepsilon} \rfloor\right), \tag{6}$$

where $\lfloor \ldots \rfloor$ is a 'floor' operation, and the values A_2, A_4 and A_8 are defined as

$$A_2 = 2^{-2r} \left| \frac{S_2}{N_e} \right|, \tag{7}$$

$$A_4 = 2^{-r} \left| \frac{2S_4}{N_e} \right|, \tag{8}$$

$$A_8 = \left| \frac{2S_8}{N_e} \right|, \tag{9}$$

which (in the case of a 3D domain) are computed in each direction along N_e^2 lines. The small value ε (set to 10^{-2} in Section 3 and 3×10^{-2} in Section 4) is used to avoid division-by-zero problems in uniform flow conditions. Note that either the maximum or mean of these A values can be taken, thereby generating slightly different variants of I_i and I_f. It was found *a posteriori* that considering the maximum values in each block seems to make the indicators I_i and I_f more sensitive compared to taking the mean values

(an operation that likely smears out any under-resolution effects). Therefore, only the maximum values are considered in this paper.

The quantity I_i is an integer in the set $\{0,\ 1,\ 2,\ 3\}$, where a value of 3 indicates the worst possible error according to the error indicator, and 0 indicates that no error is present. In contrast, the quantity I_f is a real value bounded below by zero (which indicates that little or no solution error is present). The I_i indicator was devised by partitioning the spectrum decay into 3 spectral amplitude 'pairs' (S_2–S_4, S_4–S_8, S_2–S_8). The ratios of these pairs give a piecewise indication of how the spectrum decays and should satisfy a maximum acceptable deviation/'turn-up' in the spectrum's slope. Any breach of these criteria is penalised accordingly, with a similar approach also being applied to I_f:

$$\left|\frac{S_2}{S_4}\right| \leq 2^r, \tag{10}$$

$$\left|\frac{S_4}{S_8}\right| \leq 2^{r+1}, \tag{11}$$

$$\left|\frac{S_2}{S_8}\right| \leq 2^{2r+1}. \tag{12}$$

Deciding what constitutes an unacceptably high 'turn-up' in the spectrum's slope depends on the specific problem at hand. One of the caveats of the approach is the need to estimate the minimal acceptable slope r of the spectrum. For example, this could be taken to decrease with a slope of r=-5/6 for turbulent dynamics (following Kolomogorov's $k^{-5/3}$ law for the inertial subrange of the spectral energy spectrum), but in practise r will be higher or lower locally; throughout this paper we consider a slope value of r

= -0.5. If shocks are present, then a slope of -1 (following the k^{-2} law for discontinuities [18]) may be more appropriate. Note also that the slope r may also depend on the behaviour of the solution field/quantity being considered. The typical values mentioned so far correspond to the decay of energy, but it was found *a posteriori* that these values also worked well for vorticity which followed a similar decay pattern. Nevertheless, it is important to remember that the desired slope may vary depending on the chosen quantity and problem.

The current approach is different to error indicators already appearing in the literature. For example, robust indicators that are based on the second derivative (such as the Hessian matrix [19, 20]) or interior penalty methods [21] could also be used. However, one potential caveat with second derivative-based methods occurs when the solution has a low second derivative but still shows a 'turn-up' in the Fourier spectrum decay. A flat spectrum without any 'turn-up' in the Fourier amplitude would pass our measure but fail the Hessian measure. Conversely, a steep spectrum with a 'turn-up' would pass the Hessian measure but fail our measure. Moreover, the way our approach analyses solution error mimics the way a user would manually check flow fields for grid-to-grid point oscillations and refine as necessary.

3. Test Case: Compressible Taylor-Green Vortex

A three-dimensional compressible Taylor-Vortex problem (see e.g. [16]) in a periodic cube domain of length 2π was used to evaluate the effectiveness of the error indicator. This considered a fourth-order finite difference solution without additional filtering on computational grids of size $N = 32^3$, 64^3, 128^3

and 256^3. The robustness of the error indicator was improved by considering overlapping blocks, with the grid point count per block remaining the same. The number of blocks in each direction was set to 7 such that each block contained $(N/4)^3$ solution points. This provided an error severity value every $N_e/2$ points in all directions. The N=32^3 case adopted a non-dimensional time-step Δt of 6.77×10^{-3} [16]. As the grid was refined, the time-step size was halved. The simulation was run until non-dimensional time $T = 20$. All simulations considered here were performed on a single NVIDIA Tesla K40c GPU. Further details of the simulation setup can be found in [15], where it is shown that a grid of at least 256^3 points should be employed to give close agreement with reference data [22].

The indicator computed the severity of under-resolution in the z-component of the vorticity field, denoted $(\nabla \times \mathbf{u})_z$, every 100 iterations. The 32^3 grid greatly under-resolved the turbulent dynamics and, particularly around the point of peak enstrophy, displayed grid-to-grid point oscillations as a result. As the grid was refined the overall severity of the solution error was reduced. This is reflected by the reduction in the Fourier amplitude slope in Figure 1, and also in Table 1 which shows a reduction in the maximum values of I_i and I_f across both space and time. The small increase of I_f in the 64^3 case was caused by an intermittently-high severity value at early times ($t =$ 5–6); an even larger value of ε would be required to suppress this anomalous behaviour.

A clearer visualisation is provided in Figure 2 which displays a general reduction in the number of high severity values of I_i throughout time. Larger errors were particularly noticeable around non-dimensional time $t = 9$–10 at

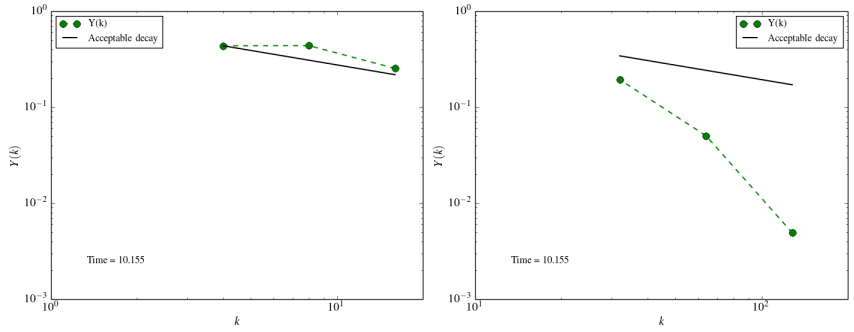

Figure 1: Comparison of Fourier amplitudes computed along a representative line of solution points in a 32^3 and 256^3 simulation near the point of peak enstrophy. The 32^3 case severely under-resolved the dynamics and the Fourier amplitude fails to decrease at the desired minimum rate, whereas the well-resolved 256^3 case demonstrates an acceptable rate of decay.

Grid size	$\max(I_i)$	$\max(I_f)$
32^3	3	1.945910
64^3	3	2.197225
128^3	2	1.386294
256^3	1	0.693147

Table 1: Grid sizes considered in the Taylor-Green vortex simulation and the maximum severity value of the error indicators over all I/O dumps.

the point of peak enstrophy where the flow becomes fully turbulent, suggesting that further grid refinement is necessary to properly resolve the turbulent fluctuations. Due to the symmetry of the problem and the domain-wide turbulence, refinement is often shown to be necessary in large portions or even all of the domain; the real benefits of error indicators and their coupling with

grid refinement techniques will become apparent when such an approach is applied to more realistic flow problems where turbulent dynamics that require higher resolution may only be present in a small section of the domain.

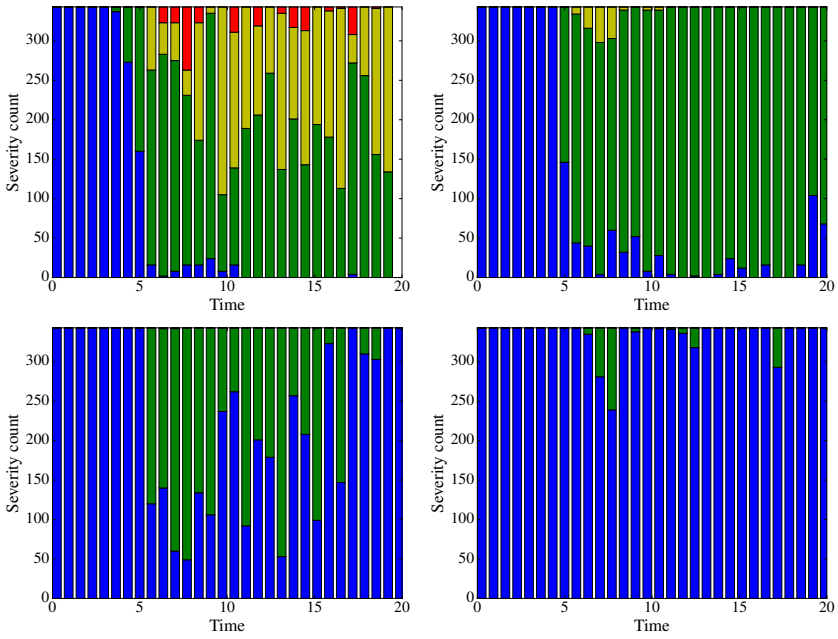

Figure 2: The counts of all the error indicator values across the entire domain for 32^3, 64^3, 128^3 and 256^3 grids (top-left to bottom-right), using overlapping blocks. Blue, green, yellow and red indicate I_i error severity values of 0, 1, 2 and 3, respectively.

4. Application: V2C laminar flow aerofoil

The error indicator was applied to a three-dimensional direct numerical simulation of transonic, compressible flow past a V2C laminar flow aerofoil (a profile designed by Dassault Aviation [17]) at an incidence $\alpha = 4°$, Reynolds number based on the aerofoil chord $Re_c = 5 \times 10^5$ and Mach number $M = 0.7$.

The computational domain is illustrated in Figure 3 and partitioned into three blocks, with interface boundary conditions between neighbouring blocks. The domain dimensions are $R = 7.5c$ and $W = 6c$ with a spanwise extension of $L_z = 0.05c$. Blocks 1 and 3 are associated with Cartesian grids stretched in the x and y directions such that more resolution is present near the trailing edge of the aerofoil and in the wake. Block 2 contains the aerofoil itself and is associated with a C-grid, with resolution being focused near the leading and trailing edges and near the wall.

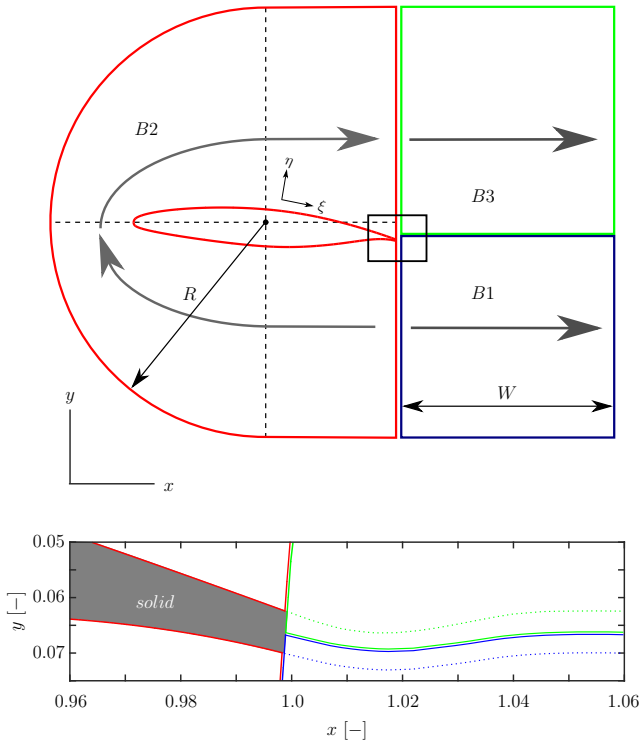

Figure 3: Sketch of the computational domain. Block 2 (denoted B2) contains the V2C aerofoil, while blocks 1 and 3 (B1 and B3) are resolving the wake line.

The V2C aerofoil profile has a blunt trailing edge and therefore two singu-

lar points at the corners. The grid points resolving the trailing edge surface are contained in blocks 1 and 3. The grid lines containing the corners of the blunt trailing edge are designed as a continuous extension of the aerofoil geometry. A corner treatment is applied according to the trailing edge treatment used by Jones [23]. In order to increase the numerical stability of supersonic flows, a total variation diminishing (TVD) scheme is applied to capture shock waves. Characteristic conditions were enforced at all the domain boundaries in order to minimise wave reflections. In particular, a zonal characteristic boundary condition [24] is applied over a distance $L_{zonal} \approx 0.45c$ near the outflow boundary of blocks 1 and 3, using 51 grid points. An integral characteristic condition [25] is applied at the other boundaries where, in addition, the free-stream solution is imposed at each time-step. The aerofoil is modelled using a no-slip, isothermal boundary condition, with the wall temperature equal to the free-stream temperature.

A summary of the two computational grids employed is given in Table 2; the first is relatively coarse, and the second is a refined version with more resolution placed near laminar-turbulent transition regions and along the wake path. The two simulations were carried out on the UK National Supercomputing Service (ARCHER). Fourth-order central differences with a Carpenter scheme near boundaries [26], and a third-order low-storage Runge-Kutta timestepping scheme (with a time step of $\Delta t = 2 \times 10^{-5}$), were used.

The error indicator implemented in the OpenSBLI code was once again applied to the z-component of the vorticity field. However, the simulation itself was performed using the legacy Fortran-based SBLI code [27] (because characteristic boundary conditions were not available in OpenSBLI at the

R/c	W/c	L_z/c	$N_{\xi,2}$	$N_{\eta,2}$	$N_{\xi,1/3}$	$N_{\eta,1/3}$	N_z	N_{total}
7.5	6.0	0.05	2095	999	999	1023	50	2.07×10^8
7.5	6.0	0.05	3045	999	1999	1023	150	1.07×10^9

Table 2: Numerical grid details for the grid before (first row) and after refinement (second row). Note that $N_{\xi,2}$ and $N_{\eta,2}$ are the number of grid points of block 2 around the aerofoil in the ξ and η direction, respectively, whereas $N_{\xi,1/3}$ and $N_{\eta,1/3}$ denote the number of grid points in block 1 and block 3 to resolve the wake (see Figure 3). N_z is the spanwise resolution and N_{total} denotes the total number of grid points.

time of writing) and the solution fields were read into OpenSBLI from a binary file. Each error indicator block comprised 16^3 grid points.

Error severity values of I_i near the aerofoil when the flow was fully developed are shown in Figure 4. The uniform flow away from the aerofoil is relatively well-resolved by both grids as suggested by I_i values of 0 or 1. The flow dynamics in the vicinity of the aerofoil are characterised by a separation of the laminar boundary layer on both sides of the aerofoil, followed by a laminar-turbulent transition of the separated flow and turbulent flow reattachment just downstream of the mid-chord position. The process of turbulent flow separation/reattachment gives rise to a highly unsteady wake downstream of the aerofoil. In the case of the coarse grid, a significant number of $I_i = 2$ and $I_i = 3$ values suggested that these latter areas of the domain exhibiting turbulent dynamics were heavily under-resolved. The grid was therefore manually refined around the trailing edge of the aerofoil and in the wake region, which resulted in a reduction in error severity (the presence of mainly $I_i = 0$ and $I_i = 1$ values) and the adequate resolution of

the turbulent structures. This demonstrates how the error indicator can be used to help target refinement strategies.

The dominant flow structures in the transitional separation region on either side of the aerofoil are represented by Kelvin-Helmholtz rollers. The interaction between these structures and the trailing edge leads to the scattering of acoustic waves that sustain the laminar-turbulent transition. The global modes caused by these acoustic waves are likely to be the cause of the occasional $I_i = 1$ values away from the aerofoil where the flow appears to be uniform. The cluster of $I_i = 2$ and $I_i = 3$ values at the leading edge is due to the thin boundary layer and has been addressed with a combination of further grid refinement and localised filtering.

5. Conclusion

A new error indicator has been developed for the purpose of determining where grid refinement needs to take place in order to ensure solution accuracy and stability in finite difference solutions of partial differential equations, here the compressible Navier-Stokes equations. It was found that both versions of the indicator (integer-based and floating point-based) correctly demonstrated a reduction in error severity when the grid was refined uniformly in a three-dimensional Taylor-Green vortex test case. Its application to a V2C industrial use case further demonstrated its usefulness by suggesting that grid refinement was particularly necessary at the trailing edge of the aerofoil where turbulent eddy shedding occurs and along the wake path. The indicator developed in this paper could potentially be used in conjunction with adaptive grid refinement techniques to dynamically alter the resolution as a

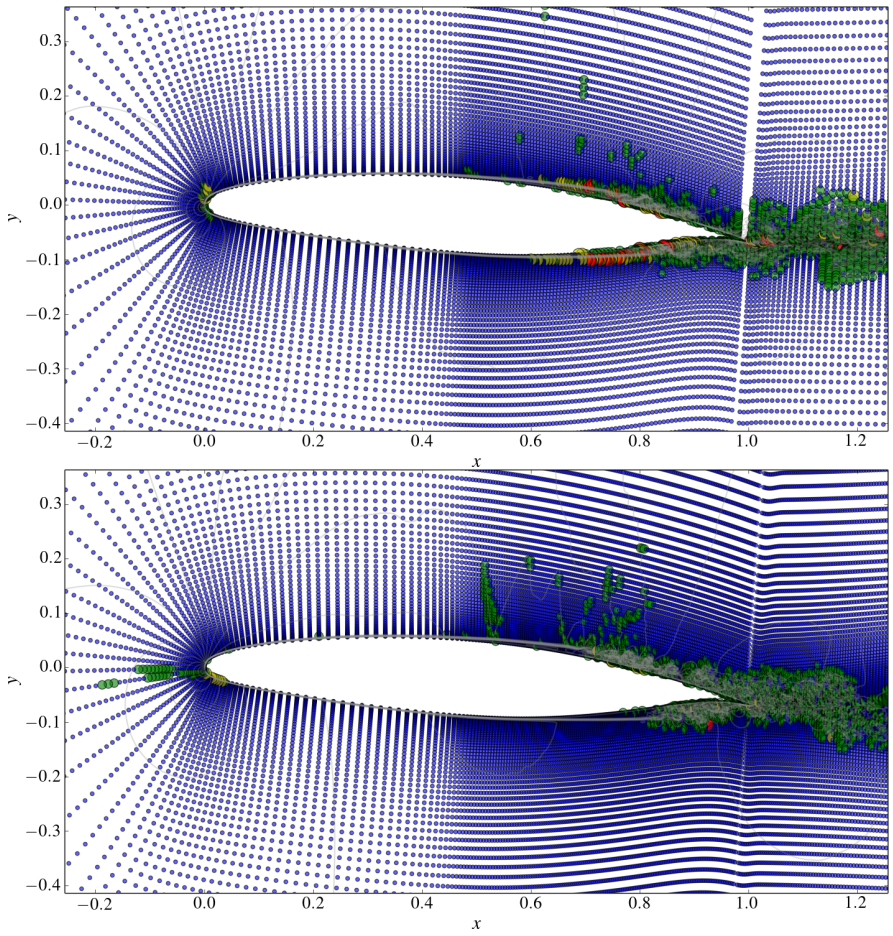

Figure 4: Contours of velocity magnitude in a two-dimensional slice of the V2C aerofoil simulation, for the initial grid (top) and the refined grid (bottom). Circles filled with blue, green, yellow and red indicate I_i error severity values of 0, 1, 2 and 3, respectively. The slices are taken at different times (after 5.33×10^6 and 6.18×10^6 timesteps, respectively).

simulation progresses, thereby enhancing the efficiency of the model.

6. Acknowledgments

CTJ and SPJ were supported by a European Commission Horizon 2020 project grant entitled "ExaFLOW: Enabling Exascale Fluid Dynamics Simulations" (671571). DJL was supported by an EPSRC Centre for Doctoral Training grant (EP/L015382/1). NDT was supported by an EPSRC grant entitled "Unsteady aerodynamics of wings in extreme conditions" (EP/M022692/1). Computer time was provided by an ARCHER Leadership grant entitled "Transonic flow over an aerofoil" (e509). The data behind the results presented in this paper will be available from the University of Southampton's institutional repository. The authors thank the NVIDIA Corporation for donating the Tesla K40c GPU used for this research.

References

[1] A. E. Honein, P. Moin, Higher entropy conservation and numerical stability of compressible turbulence simulations, Journal of Computational Physics 201 (2) (2004) 531–545. doi:10.1016/j.jcp.2004.06.006.

[2] I. Babuška, W. C. Rheinboldt, A-posteriori error estimates for the finite element method, International Journal for Numerical Methods in Engineering 12 (10) (1978) 1597–1615. doi:10.1002/nme.1620121010.

[3] I. Babuška, A. Miller, A feedback finite element method with a posteriori error estimation: Part I. The finite element method and some basic properties of the a posteriori error estimator, Computer Methods in Applied Mechanics and Engineering 12 (10) (1987) 1597–1615. doi:10.1016/0045-7825(87)90114-9.

[4] O. C. Zienkiewicz, J. Z. Zhu, A simple error estimator and adaptive procedure for practical engineerng analysis, International Journal for Numerical Methods in Engineering 24 (2) (1987) 337–357. doi:10.1002/nme.1620240206.

[5] C. Mavriplis, A Posteriori Error Estimators for Adaptive Spectral Element Techniques, Vieweg+Teubner Verlag, Wiesbaden, 1990, pp. 333–342. doi:10.1007/978-3-663-13975-1_34.

[6] M. Ainsworth, J. T. Oden, A posteriori error estimation in finite element analysis, Computer Methods in Applied Mechanics and Engineering 142 (1–2) (1997) 1–88. doi:10.1016/S0045-7825(96)01107-3.

[7] J. Peraire, M. Vahdati, K. Morgan, O. C. Zienkiewicz, Adaptive remeshing for compressible flow computations, Journal of Computational Physics 72 (2) (1987) 449–466. doi:10.1016/0021-9991(87)90093-3.

[8] R. Löhner, An adaptive finite element solver for transient problems with moving bodies, Computers and Structures 30 (1) (1988) 303–317. doi:10.1016/0045-7949(88)90236-2.

[9] R. Löhner, Three-dimensional fluid-structure interaction using a finite element solver and adaptive remeshing, Computing Systems in Engineering 1 (2) (1990) 257–272. doi:10.1016/0956-0521(90)90012-A.

[10] C. C. Pain, A. P. Umpleby, C. R. E. de Oliveira, A. J. H. Goddard, Tetrahedral mesh optimisation and adaptivity for steady-state and transient finite element calculations, Computer Methods in Applied Mechan-

ics and Engineering 190 (29-30) (2001) 3771–3796. doi:10.1016/S0045-7825(00)00294-2.

[11] M. J. Berger, P. Colella, Local adaptive mesh refinement for shock hydrodynamics, Journal of Computational Physics 82 (1) (1989) 64–84. doi:10.1016/0021-9991(89)90035-1.

[12] J. Behrens, M. Bader, Efficiency considerations in triangular adaptive mesh refinement, Philosophical Transactions of the Royal Society A 367 (1907) (2009) 4577–4589. doi:10.1098/rsta.2009.0175.

[13] M. T. Jones, P. E. Plassmann, Parallel Algorithms for Adaptive Mesh Refinement, SIAM Journal on Scientific Computing 18 (3) (1997) 686–708. doi:10.1137/S106482759528065X.

[14] S. Pirozzoli, Numerical Methods for High-Speed Flows, Annual Review of Fluid Mechanics 43 (1) (2011) 163–194.

[15] C. T. Jacobs, S. P. Jammy, N. D. Sandham, OpenSBLI: A framework for the automated derivation and parallel execution of finite difference solvers on a range of computer architectures, Journal of Computational Science 18 (2017) 12–23. doi:10.1016/j.jocs.2016.11.001.

[16] J. DeBonis, Solutions of the Taylor-Green Vortex Problem Using High-Resolution Explicit Finite Difference Methods, in: 51st AIAA Aerospace Sciences Meeting including the New Horizons Forum and Aerospace Exposition, Aerospace Sciences Meetings, 2013. doi:10.2514/6.2013-382.

[17] J. Sznajder, T. Kwiatkowski, Analysis of effects of shape and location of micro-turbulators on unsteady shockwave-boundary layer interaction

in transonic flow, in: Proceedings of the VII European Congress on Computational Methods in Applied Sciences and Engineering, 2016.

[18] J. P. Boyd, The Energy Spectrum of Fronts: Time Evolution of Shocks in Burgers' Equation, J. Atmos. Sci 49 (2) (1992) 128–139.

[19] G. C. Buscaglia, E. A. Dari, Anisotropic mesh optimization and its application in adaptivity, International Journal for Numerical Methods in Engineering 40 (22) (1997) 4119–4136. doi:10.1002/(SICI)1097-0207(19971130)40:22¡4119::AID-NME254¿3.0.CO;2-R.
URL http://dx.doi.org/10.1002/(SICI)1097-0207(19971130)40:22<4119::AID-NME254

[20] K. Lipnikov, Y. Vassilevski, Error Estimates for Hessian-Based Mesh Adaptation Algorithms with Control of Adaptivity, in: 13th International Meshing Roundtable, Williamsburg, Virginia, USA, 2004. doi:10.2514/6.2014-3210.

[21] C. Dawson, J. Proft, A priori error estimates for interior penalty versions of the local discontinuous Galerkin method applied to transport equations, Numerical Methods for Partial Differential Equations 17 (6) (2001) 545–564. doi:10.1002/num.1026.
URL http://dx.doi.org/10.1002/num.1026

[22] Z. Wang, K. Fidkowski, R. Abgrall, F. Bassi, D. Caraeni, A. Cary, H. Deconinck, R. Hartmann, K. Hillewaert, H. Huynh, N. Kroll, G. May, P.-O. Persson, B. van Leer, M. Visbal, High-order CFD methods: current status and perspective, International Journal for Numerical Methods in Fluids 72 (8) (2013) 811–845. doi:10.1002/fld.3767.

[23] L. E. Jones, Numerical studies of the flow around an airfoil at low Reynolds number, Ph.D. thesis, University of Southampton (2008).

[24] R. Sandberg, N. Sandham, Nonreflecting zonal characteristic boundary condition for direct numerical simulation of aerodynamic sound, AIAA J. 44 (2) (2006) 402–405.

[25] H. Sandhu, N. D. Sandham, Boundary conditions for spatially growing compressible shear layers, Report QMW-EP-1100, Faculty of Engineering, Queen Mary and Westfield College, University of London (1994).

[26] M. H. Carpenter, D. Gottlieb, S. Abarbanel, Time-Stable Boundary Conditions for Finite-Difference Schemes Solving Hyperbolic Systems: Methodology and Application to High-Order Compact Schemes, Journal of Computational Physics 111 (2) (1994) 220–236.

[27] Y. Yao, Z. Shang, J. Castagna, N. D. Sandham, R. Johnstone, R. D. Sandberg, V. Suponitsky, J. A. Redford, L. E. Jones, N. De Tullio, Re-Engineering a DNS Code for High-Performance Computation of Turbulent Flows, in: Proceedings of the 47th AIAA Aerospace Sciences Meeting including The New Horizons Forum and Aerospace Exposition, Aerospace Sciences Meetings, 2009. doi:10.2514/6.2009-566.